Available online at www.sciencedirect.com
ScienceDirect
Trans. Nonferrous Met. Soc. China 35(2025) 563−578

Transactions of
Nonferrous Metals
Society of China
www.tnmsc.cn

Defect-engineered rGO−$CoNi_2S_4$ with enhanced electrochemical performance for asymmetric supercapacitor

Xu WANG[1], Bo-wang ZHAO[1], Jia-yu LIANG[1], Geng-zheng LIU[1],
Ze-fei GUO[1], Hui-lian HAO[1], Wen-yao LI[1], Wen-zhong SHEN[2]

1. College of Materials Materials Science and Engineering, Shanghai University of Engineering Science,
Shanghai 201620, China;
2. School of Physics and Astronomy, Shanghai Jiao Tong University, Shanghai 200240, China

Received 5 July 2023; accepted 26 March 2024

Abstract: To explore the effect of sulfur vacancies in transition metal sulfide on the electrochemical properties of anode materials, the graphene oxide (GO) and $CoNi_2S_4$ were used as the raw materials to synthesize the rGO_{10}−$CoNi_2S_{4-x}$ composite electrode materials by the solvothermal method. The obtained rGO_{10}−$CoNi_2S_{4-x}$ electrode materials with sulfur vacancies consist of nanoflakes and nanorods. The galvanostatic charge−discharge test of the rGO_{10}−$CoNi_2S_{4-x}$ electrode materials shows a great specific capacitance of 3050.1 F/g at a current density of 1 A/g. Moreover, the electrode materials still remain rate capability retention of 86.1% when the current density increases from 1 to at 10 A/g. The rGO_{10}−$CoNi_2S_{4-x}$ composite containing sulfur vacancies has higher specific capacitance and better rate capability in comparison to the pristine rGO−$CoNi_2S_4$ without containing sulfur defects. The optimized rGO_{10}−$CoNi_2S_{4-x}$ composite electrode materials with sulfur vacancies exhibit outstanding cycle stability and rate performance.

Key words: rGO_{10}−$CoNi_2S_{4-x}$ composite; supercapacitor; electrochemical performance; sulfur vacancy; solvothermal method

---

1 Introduction

In recent years, considerable research has been conducted for searching the eco-friendly and high-efficiency electrochemical energy storage systems [1−3]. Supercapacitors (SCs), the novel form of energy storage devices with high power density, lying between batteries and conventional capacitors, have a potential application in the energy storage. However, SCs have a lower energy density, which severely hinders their widespread applications. Consequently, it is urgent to develop SCs with a high energy density to meet the requirements of energy storage devices. It is well known that the electrochemical performance of SCs relies heavily on the characteristics of electrode materials, among which the transition metal sulfides have recently attracted much attention, due to their superior thermal stability, high theoretical capacitance, and exceptional electrical conductivity [3,4]. The nano-structured transition metal sulfides usually present prominent electrochemical properties. XU et al [5] synthesized partially amorphous $CoNi_2S_4$ nanosheets by a facile solvothermal method, which delivered a specific capacitance (C_s) of 3350 F/g at current density of 2 A/g. LIU et al [6] synthesized the uniformly reduced $CoNi_2S_4$ (r-$CoNi_2S_4$) nanosheets containing sulfur vacancies using a one-step hydrolysis process. The fabricated r-$CoNi_2S_4$ achieved C_s of 1918.9 F/g at 1 A/g and retained 76.2% of its original capacity after 10000 cycles. The formation of sulfur vacancies can significantly increase the number of sites and reduce the Gibbs

---

Corresponding author: Hui-lian HAO, Tel: +86-21-67791380, E-mail: sulee8866@126.com

DOI: https://doi.org/10.1016/S1003-6326(24)66700-2

1003-6326/© 2025 The Nonferrous Metals Society of China. Published by Elsevier Ltd & Science Press
This is an open access article under the CC BY-NC-ND license (http://creativecommons.org/licenses/by-nc-nd/4.0/)

free energy of surface reactions, leading to the effective redox reactions [7,8]. However, transition metal sulfides are susceptible to agglomerate during charging−discharging processes, resulting in the reduction of surface area and active spots [9]. Thus, it is urgent to fabricate the electrode materials with outstanding electrochemical properties to satisfy the requirement of the high-performance supercapacitors. Defect engineering has been proven to be an efficient technique for creating active sites in transition metal sulfides and enhancing their intrinsic electrical conductivity [10,11]. The formation of sulfur vacancies in transition metal sulfides has been anticipated to increase the number of binding sites and conductivity, thus boosting the electrochemical properties [12,13].

Enhancing the conductivity and ion diffusion of transition metal sulfides can promote the charge transfer of electrode materials [14]. It is well known that the reduced graphene oxide (rGO) features with high conductivity and large specific surface area [9]. It is expected that the incorporation of low dimension and large specific surface area rGO into the electrode materials can further ameliorate the conductivity, ions diffusion rate and accessible surface areas of the faradic electrodes, which are essential factors to facilitate sufficient faradic reactions, therefore increasing the capacities of electrodes and devices. Additionally, the high dispersity of graphene oxide (GO) precursor can afford faradic composites, which can satisfy the comprehensive electrical performance demands in more widespread facilities.

In this work, the introduction of sulfur vacancies and rGO substantially enhances the faradic activity of the synthesized composite of rGO and $CoNi_2S_4$ (rGO−$CoNi_2S_4$) and restrains the agglomeration of transition metal sulfides during charge−discharge process to some degree. In addition, owing to the strong reduction characteristic of $NaBH_4$, the obtained rGO−$CoNi_2S_4$ composite materials with sulfur vacancies preserve more reactive sites and low Gibbs free energy change, which can promote the electrochemical reactions and improve the electrochemical performance of the device. This research is expected to provide a theoretical and experimental basis for the research of transition metal sulfide electrode materials.

2 Experimental

2.1 Materials synthesis

The Ni−Co precursors were synthesized by a typical solvothermal method. In brief, 291.0 mg $Co(NO_3)_2\cdot6H_2O$ and 582.0 mg $Ni(NO_3)_2\cdot6H_2O$ were uniformly dissolved in the mixed solvent of ethylene glycol (EG) and deionized (DI) water (60 mL, $V_{EG}:V_{DI}=3:1$) by stirring for 30 min. Then, 378.2 mg $C_2H_2O_4\cdot2H_2O$ was slowly added into the above mixed solution under continuous stirring until it was completely dissolved to obtain the transparent mixture. The obtained mixture was subsequently transferred to an autoclave and treated hydrothermally for 24 h at 120 °C. Next, the reactants were cooled to 25 °C and cleaned with DI water and alcohol several times. The Ni−Co precursors were finally obtained by vacuum freeze-drying at −60 °C for 24 h.

GO was produced by the reported Hummers procedure. The rGO−$CoNi_2S_4$ composite with different GO masses was synthesized as follows: 300 mg Ni−Co precursor and a certain amount of GO were dispersed in the mixed solvent of EG (30 mL) and DI water (30 mL), and the uniform dispersion was achieved after 30 min ultrasonic treatment. Then, 300 mg $Na_2S\cdot9H_2O$ was added into the above dispersion and kept in a high-pressure reactor at 120 °C for 6 h to achieve the rGO−$CoNi_2S_4$ nanoflakes. The obtained composites were named as rGO_n−$CoNi_2S_4$ with different GO masses (n=0, 5, 10, 20 and 40 mg). The prepared rGO_n−$CoNi_2S_4$ samples were reduced by submerging in 0.9 mol/L $NaBH_4$ solution and placed at ambient temperature for 30 min to obtain rGO−$CoNi_2S_4$ with sulfur vacancies named as rGO_n−$CoNi_2S_{4-x}$ nanosheets. The preparation schematic diagram of rGO_n−$CoNi_2S_{4-x}$ composite material is shown in Fig. 1.

2.2 Material characterization

The structures of all the synthesized samples were analyzed using Raman spectroscopy (Raman, Horiba evolution), transmission electron microscopy (TEM, F200X), X-ray photoelectron spectroscopy (XPS, Thermo Scientific K-Alpha), scanning electron microscopy (SEM, ZEISS Gemini 300), X-ray diffraction (XRD, X’Pert PRO), electron

Fig. 1 Schematic illustration of synthesis of rGO$_n$−CoNi$_2$S$_{4-x}$

paramagnetic resonance (EPR, Bruker EMplus−6/1), and Brunauer−Emmet−Teller analyzer (BET, Micromeritics, JW-BK112T).

2.3 Electrochemical measurements

Electrochemical tests of all the as-prepared samples were performed using an electrochemical workstation (CHI660E, Shanghai, China) with a three-electrode setup. The three electrodes were working electrode, reference electrode and counter electrode, corresponding to the as-prepared electrode materials, Hg/HgO and platinum, respectively. Galvanostatic charge−discharge (GCD), electrochemical impedance spectroscopy (EIS), and cyclic voltammetry (CV) measurements were developed to assess the capabilities of electrode materials. The nickel foam (NF) was immersed in the mixture of HCl and ethanol solution to sonicate for 15 min, following vacuum-drying at 50 °C for 12 h. The pretreated NF was coated with the semi-solid slurry of the active material, acetylene black conductor, and polyvinylidene fluoride with a mass ratio of 8:1:1. Finally, the coated NF was dried at 60 °C for 12 h. Each electrode had about 1 cm × 1 cm loading area and the electrolyte was 3 mol/L KOH.

3 Results and discussion

3.1 Microstructure of electrode materials

SEM was used to observe the morphological structures of the electrode materials. Figure 2(a) displays the image of the Co−Ni precursors, which exhibits the interlaced linear structure with diameters of 100−200 nm. The micrograph of rGO in Fig. 2(b) displays an ultra-thin pleated structure. The uniformly sized CoNi$_2$S$_4$ in Fig. 2(c) originates from the Co−Ni precursors after the sulfidation process, and the original geometry of Co−Ni precursors is well preserved. Figure 2(d) shows the SEM image of rGO$_{10}$−CoNi$_2$S$_{4-x}$ electrode, which exhibits a novel structure containing both nanoflakes and nanorods. The rGO$_{10}$−CoNi$_2$S$_{4-x}$ presents smaller size and more irregular morphology, which is probably because the nuclei formation and crystal growth of the CoNi$_2$S$_4$ are affected by the groups of rGO during the reaction. It should be noted that the nanorods of CoNi$_2$S$_4$ are largely coated with rGO, which can serve as the protective layer to inhibit the severe volume variations during repeated electrochemical cycles, and therefore to improve the cycle ability of the electrode. Meanwhile, the surface of the rGO$_{10}$−CoNi$_2$S$_{4-x}$ becomes rougher compared with that of CoNi$_2$S$_4$, suggesting the larger specific surface area. The obtained rGO$_{10}$−CoNi$_2$S$_{4-x}$ nanosheets still maintain partially open sheet structure, which is beneficial to rGO$_{10}$−CoNi$_2$S$_{4-x}$ to shorten the ion diffusion distance and transport.

As determined by energy dispersive spectroscopy (EDS) mappings in Fig. 3, C, S, Ni, and Co components distribute uniformly throughout the rGO$_{10}$−CoNi$_2$S$_{4-x}$ nanosheets. The presence of carbon element in EDS pattern of rGO$_{10}$−CoNi$_2$S$_{4-x}$ could be the further proof of the existence of rGO. In addition, EDS patterns in Fig. S1 (Supporting Information (SI)) clearly reveal that the Ni/Co:S molar ratio is significantly increased from 0.03 in CoNi$_2$S$_4$ to 0.13 in rGO$_{10}$−CoNi$_2$S$_{4-x}$, in accordance with the presence of an extensive number of sulfur vacancies [15].

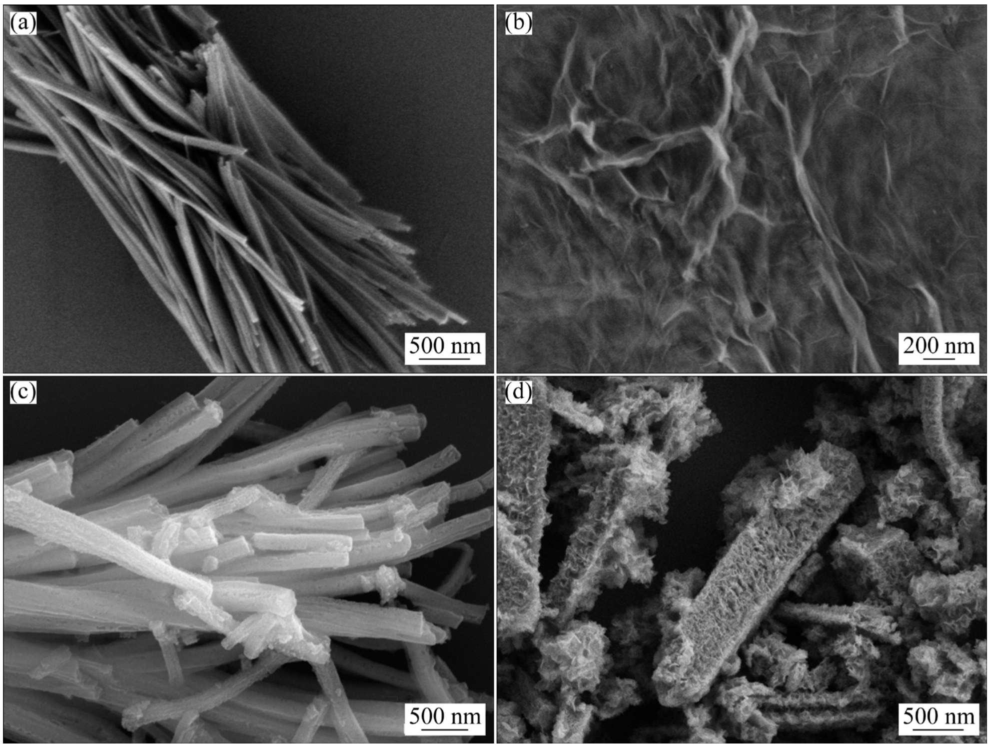

Fig. 2 SEM images of different materials: (a) Co−Ni precursor nanowires; (b) rGO; (c) Hierarchical $CoNi_2S_4$; (d) rGO_{10}−$CoNi_2S_{4-x}$

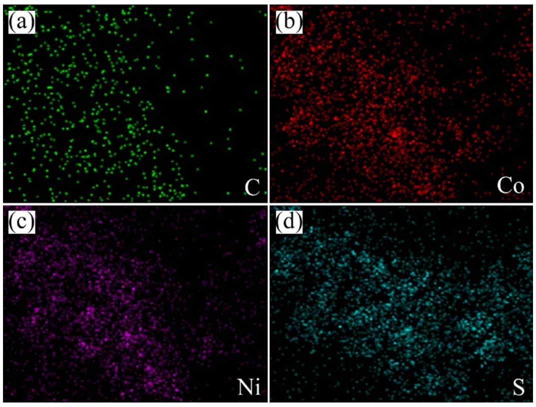

Fig. 3 EDS elemental mappings of rGO_{10}−$CoNi_2S_{4-x}$

Figure 4(a) displays the TEM image of rGO_{10}−$CoNi_2S_{4-x}$. It can be seen that rGO evenly develops on the surface of $CoNi_2S_{4-x}$, which can enhance the stability of the composite electrode material. The selected area electron diffraction (SAED) pattern of rGO_{10}−$CoNi_2S_{4-x}$ in Fig. 4(b) shows the obvious multiple rings, indicating polycrystalline structure. The interlayer spacings (provided in Table S1 in SI) correlate well to the (440), (422), (400), and (220) of the composite. Through the high-resolution transmission electron microscopy (HRTEM, Fig. 4(c)) and inverse fast Fourier transform (IFFT, Figs. 4(c_1, c_2)) images, two groups of lattice stripes with interlayer spacings of 0.28 and 0.33 nm correspond to (311) and (220) crystal planes of $CoNi_2S_4$, respectively. The above findings demonstrate the effective production of rGO_{10}−$CoNi_2S_{4-x}$.

Figure 5(a) demonstrates XRD diffraction peaks of $CoNi_2S_4$ and rGO_{10}−$CoNi_2S_{4-x}$ at 2θ values of 26.7°, 31.5°, 38.0°, and 55.0°, which are corresponding to the (220), (311), (400), and (440) lattice planes of the cubic type $CoNi_2S_4$ (JCPDS No. 20-0334), respectively, good consistent with SAED results. Moreover, the well-matched XRD diffraction peaks for two samples indicate good preservation of the $CoNi_2S_4$ crystal structure following the treatment by $NaBH_4$. To detect the intrinsic defects of the sample, EPR measurements were performed to probe the sulfur vacancies (Fig. 5(b)). The gyromagnetic factor (g) governs the magnetic splitting of unpaired electron energy levels, with the free-electron theoretical value at about 2.0023. Deviations from this benchmark reflect localized chemical environments involving crystal field effects and spin-orbit coupling. Sulfur vacancies induce symmetry reduction through localized magnetic moments, directly modifying g-values via orbital reconfiguration. The reduced rGO_{10}−$NiCo_2S_{4-x}$ sample displays an obvious signal at g=2.005, corresponding to the unpaired electrons

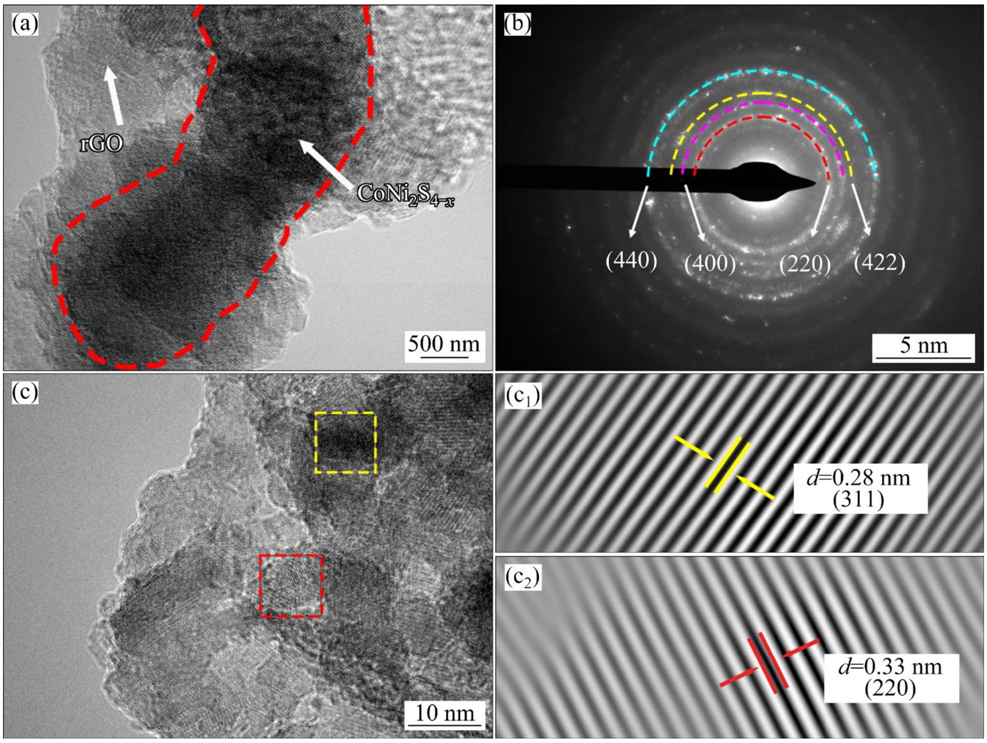

Fig. 4 Micro-morphologies of rGO_{10}−$CoNi_2S_{4-x}$: (a) TEM image; (b) SAED pattern; (c) HRTEM image; (c_1, c_2) IFFT images

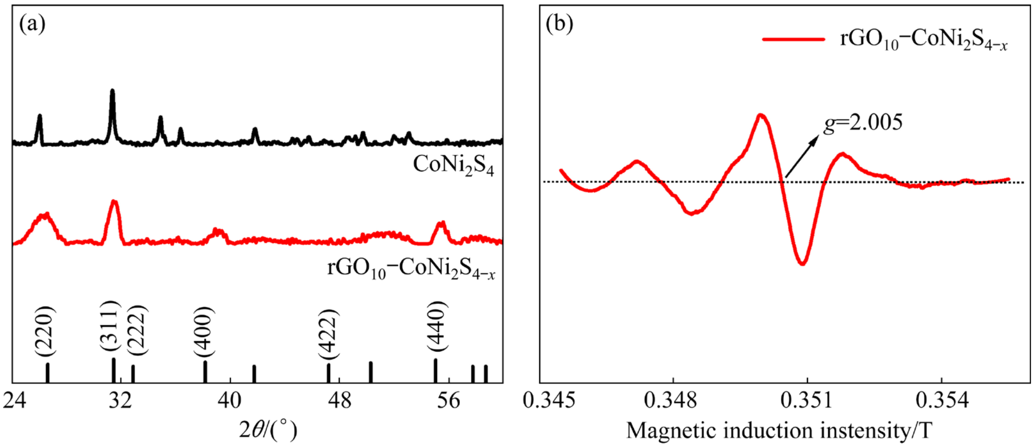

Fig. 5 XRD patterns of $CoNi_2S_4$ and rGO_{10}−$CoNi_2S_{4-x}$ (a) and EPR pattern of rGO_{10}−$CoNi_2S_{4-x}$ (b)

trapped at the sulfur vacancies in the lattice [15], which also indicates that sulfur vacancies are created during solvothermal reduction. The presence of sulfur vacancies can significantly enhance redox rate and conductivity of composites, which is particularly beneficial to energy storage applications. Figure 6(a) presents the Raman spectra of the $CoNi_2S_4$ and rGO_{10}−$NiCo_2S_{4-x}$ nanosheets. For $CoNi_2S_4$, the vibration peak at ~464 cm^{-1} is correlated to the E_g and A_g of S−S pairs in NiS_x, and the vibration peak at ~515 cm^{-1} is attributed to the S−S pair of CoS_x [16]. It can be obviously found that the above two vibration peaks weaken or even disappear in rGO_{10}−$NiCo_2S_{4-x}$ compared with those of $CoNi_2S_4$, demonstrating the reduction reaction of $CoNi_2S_4$ nanosheets and the formation of sulfur vacancies [17]. In addition, the peak located at ~515 cm^{-1} can be ascribed to the tetragonal S−Ni (Co) bands of $NiCo_2S_4$ and rGO_{10}−$NiCo_2S_{4-x}$, proving that the bimetallic sulfides have successfully grown onto the Ni foam [11]. Furthermore, the disappearance of vibration peak at ~516 cm^{-1} discloses the generation of sulfur vacancies [18]. As can be seen in Fig. 6(b), the

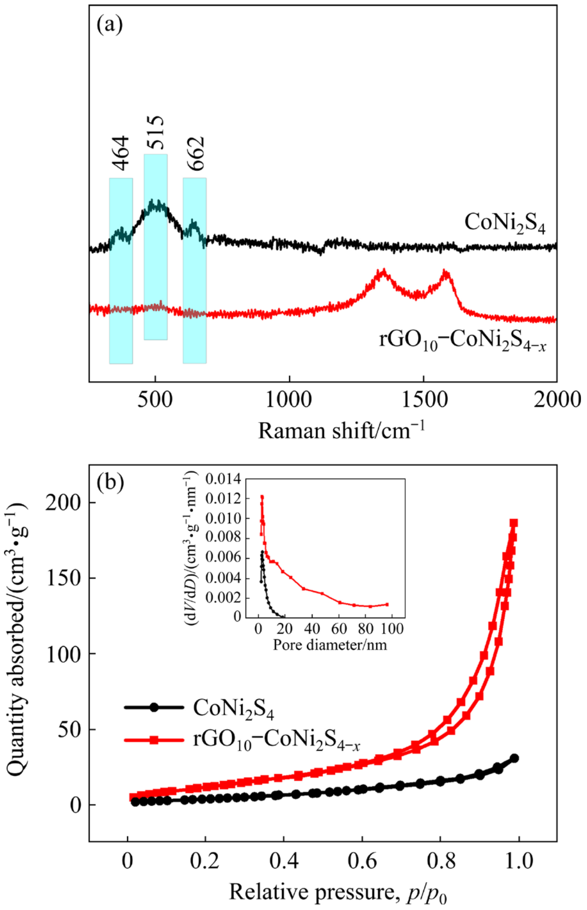

Fig. 6 Raman spectra (a) and N_2 adsorption−desorption isotherms (b) of $CoNi_2S_4$ and $rGO_{10}-CoNi_2S_{4-x}$

specific surface area and porous structure of electrode materials can be revealed by nitrogen adsorption−desorption experiments. It can be observed that both isotherms for $rGO_{10}-CoNi_2S_{4-x}$ and pure $CoNi_2S_4$ belong to IV type based on the Brunauer−Deming−Teller classification. The two obvious adsorption hysteretic loops locate at p/p_0=0.7−1.0, suggesting that both samples owe porous structure with abundant mesopores. The calculated specific surface area of $rGO_{10}-CoNi_2S_{4-x}$ is 46.777 m^2/g, which is much larger than that of $CoNi_2S_4$ (15.275 m^2/g). The inset of Fig. 6(b) illustrates the pore diameter (D) distribution according to the desorption isotherm, which is calculated based on Barret−Joyner−Halenda method. As can be seen from the inset, the sizes of mesopores lie 2−50 nm for both samples. The average pore diameter of $rGO_{10}-CoNi_2S_{4-x}$ (~24.7 nm) is much larger than that of $CoNi_2S_4$ (~12.4 nm). The above results suggest that the structure of $rGO_{10}-CoNi_2S_{4-x}$ is ideal for increasing active sites and conducive to the transport of electrolyte ions, so as to achieve excellent electrochemical performance.

The elemental structure and chemical valence states of $CoNi_2S_4$ and $rGO_{10}-CoNi_2S_{4-x}$ nanosheet arrays were analyzed by XPS characterization. As can be seen from the full XPS spectra in Fig. 7, O, Co, Ni, S, and C elements can be detected for two samples. Figures 8(a−c) illustrate the typical XPS spectra of Co 2p, Ni 2p, and S 2p generated by Gaussian fitting for both samples, respectively. The full Co 2p spectra for two samples in Fig. 8(a) feature four spin-orbit locations and two satellite peaks (identified as “Sat.”). In the Co 2p spectrum of $CoNi_2S_4$, the two main peaks locate at ~781.3 and 797.4 eV with the spin-orbit splitting energy of 16.1 eV and correspond to Co^{2+}. Meanwhile, the two peaks situate at ~ 778.3 and 793.1 eV with the spin-orbit splitting energy around 14.8 eV and correlate to Co^{3+} [6].

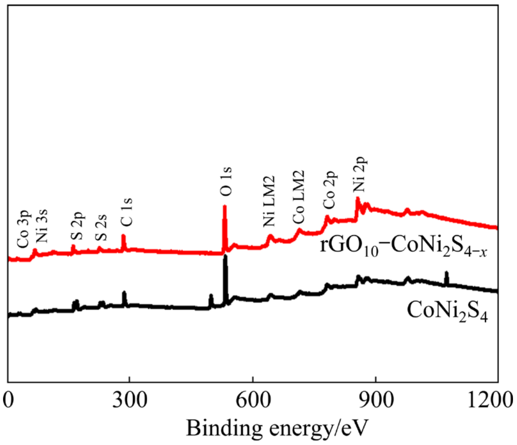

Fig. 7 XPS survey scan spectra for $CoNi_2S_4$ and $rGO_{10}-CoNi_2S_{4-x}$

Figure 8(b) shows the XPS spectra of Ni 2p for both samples. For $CoNi_2S_4$ sample, the two peaks at ~853.0 and 872.8 eV correspond to Ni^{2+}, and the double peaks at ~856.3 and 873.6 eV are related to Ni^{3+}. After $CoNi_2S_4$ sample is reduced by $NaBH_4$, the intensity of both peaks of Ni^{3+} in $rGO_{10}-CoNi_2S_{4-x}$ is much stronger than that of $CoNi_2S_4$, indicating the obvious increase of Ni^{3+} in $rGO_{10}-CoNi_2S_{4-x}$, which reveals that the content of Ni^{3+} is obviously increased. The increase of Ni^{3+} in $rGO_{10}-CoNi_2S_{4-x}$ can thereby facilitate the robust oxidation−reduction process and enhance the electrochemical properties of SCs [19]. For S 2p spectra of $CoNi_2S_4$ in Fig. 8(c), two peaks with binding energies at around 162.5 and 163.7 eV

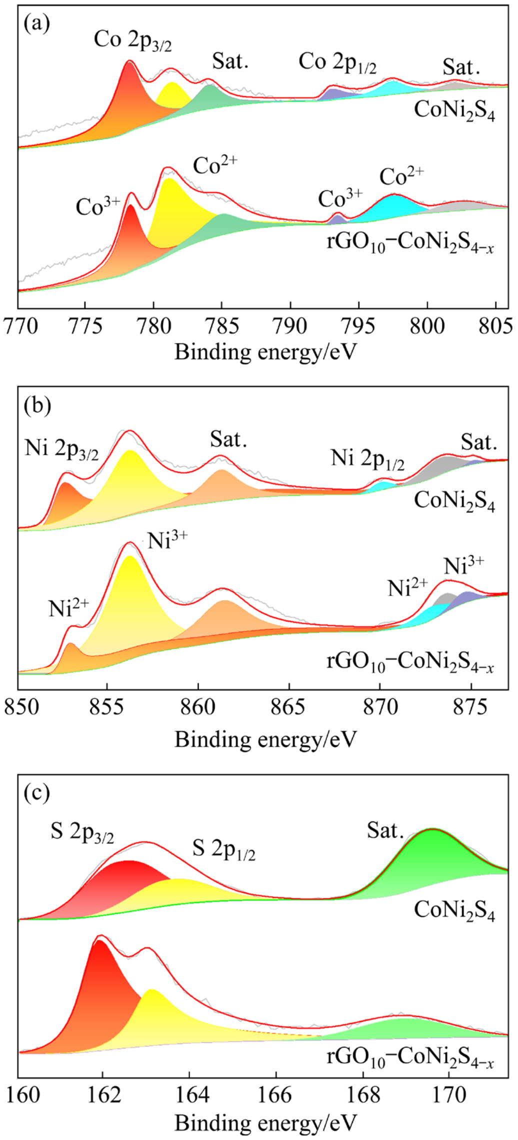

Fig. 8 XPS spectra of Co 2p (a), Ni 2p (b), and S 2p (c) of $\mathrm{CoNi_2S_4}$ and $\mathrm{rGO_{10}{-}CoNi_2S_{4-x}}$ (Sat. means satellite peak)

correspond to S $2p_{3/2}$ and S $2p_{1/2}$, respectively. In particular, the peak at 162.5 eV is ascribed to the metal sulfur bond in $\mathrm{CoNi_2S_4}$ material [20]. Compared with the S 2p spectrum of $\mathrm{CoNi_2S_4}$, the energy bands of S $2p_{3/2}$ and S $2p_{1/2}$ of $\mathrm{rGO_{10}{-}CoNi_2S_{4-x}}$ nanosheets take redshift to 161.9 and 163.1 eV, respectively, and the reduction in binding energies is attributed to the formation of sulfur vacancies [21]. According to first-principles analysis, the introduction of sulfur vacancies can considerably enhance the Fermi level of the S 2p states and charge transfer, therefore increasing the conductivity of $\mathrm{rGO_{10}{-}CoNi_2S_{4-x}}$ nanostructures [22].

3.2 Electrochemical properties of electrode materials

Figure 9(a) depicts the CV curves of the pristine Ni foam substrates, $\mathrm{CoNi_2S_4}$ and $\mathrm{rGO_{10}{-}CoNi_2S_{4-x}}$ electrode materials at a scan rate of 10 mV/s in a range of 0−0.6 V. For bare Ni foam, the closed CV curve area is almost negligible compared with that of $\mathrm{CoNi_2S_4}$ or $\mathrm{rGO_{10}{-}CoNi_2S_{4-x}}$, illustrating that the capacitor contributor can be negligible for bare Ni foam and mainly originates from $\mathrm{CoNi_2S_4}$ or $\mathrm{rGO_{10}{-}CoNi_2S_{4-x}}$. For $\mathrm{CoNi_2S_4}$ and $\mathrm{rGO_{10}{-}CoNi_2S_{4-x}}$ electrode materials, both CV curves show a pair of prominent symmetric redox peaks, the upper peaks are the oxidation peaks produced during the oxidation reaction and the lower ones are reduction peaks originating from the reduction reaction, demonstrating that the capacitance is predominant as a result of the reversible Faraday redox reaction. Due to the formation of sulfur vacancies, $\mathrm{rGO_{10}{-}CoNi_2S_{4-x}}$ composite material possesses a lager enclosed region of CV curve than $\mathrm{CoNi_2S_4}$, revealing that much more charges can be stored. In addition, the redox peaks of $\mathrm{rGO_{10}{-}CoNi_2S_{4-x}}$ show slight shifts towards more positive and negative directions compared with those of $\mathrm{CoNi_2S_4}$ under a specific scan rate, which can be attributed to the reversible redox reaction of nickel sulfide with the enhancement of $\mathrm{Ni^{3+}}$, as verified by the XPS measurements. The possible reaction based on $\mathrm{Ni^{3+}}$ can be excluded as follows: $\mathrm{NiS+OH^- \rightleftharpoons NiSOH+e}$ [22].

Figures 9(b) and S2(a) in SI illustrate the CV curves of $\mathrm{rGO_{10}{-}CoNi_2S_{4-x}}$ and $\mathrm{CoNi_2S_4}$ electrode materials in the scan rate range of 1−30 mV/s, respectively. For all CV curves, the well-defined redox peaks originate from Faradic redox. With the enhancement of scan rate, on the one hand, the current intensity increases accordingly. On the other hand, it can be seen that the anodic peaks shift towards positive potential and the cathodic peaks move to negative potential. At lower scan rates, the redox reactions usually depend on the insertion−deinsertion of ions from the electrolyte, and the diffusion of ions from the electrolyte can enter into all the effective holes of the electrode. With increasing scan rate, the effective interaction between the ions and the electrode is greatly reduced, leading to a lower areal capacitance. The shapes of CV curves remain unchanged even at a

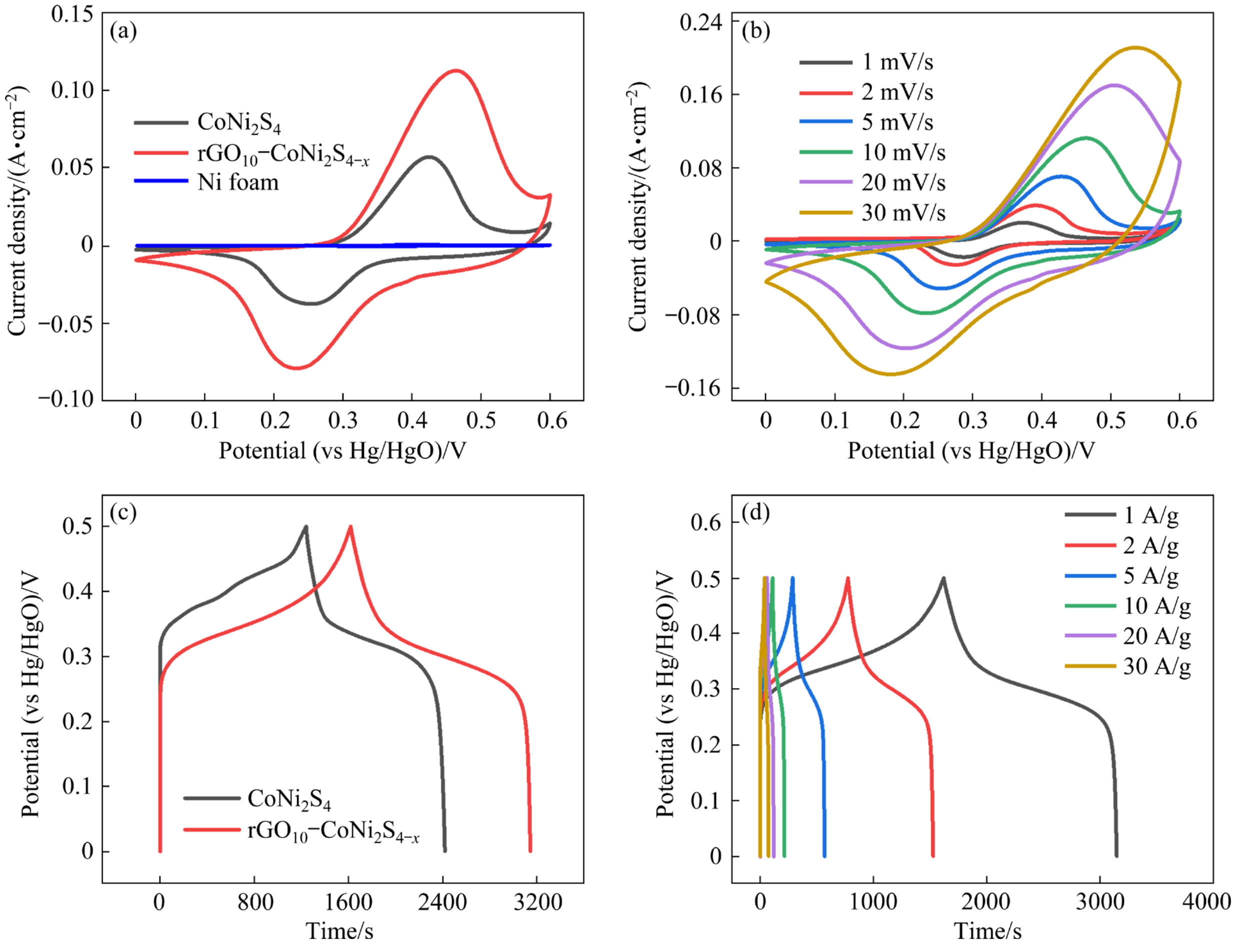

Fig. 9 CV curves of Ni foam, $CoNi_2S_4$ and $rGO_{10}-CoNi_2S_{4-x}$ at scan rate of 10 mV/s in 3 mol/L KOH electrolyte (a), CV curves of $rGO_{10}-CoNi_2S_{4-x}$ in scan rate range 1−30 mV/s (b), GCD curves of $CoNi_2S_4$ and $rGO_{10}-CoNi_2S_{4-x}$ at 1 A/g (c), and GCD curves of $rGO_{10}-CoNi_2S_{4-x}$ in current density range of 1−30 A/g (d)

scan rate as high as 30 mV/s, implying excellent reversibility and superior reaction kinetics. It should be noted that the closed CV curve area of $rGO_{10}-CoNi_2S_{4-x}$ is much larger than that of $CoNi_2S_4$ at the corresponding scan rate, indicating much higher C_s. This can be attributed to the formed sulfur vacancies in $rGO_{10}-CoNi_2S_{4-x}$ as proved by EPR measurements, which is conducive to promoting rapid redox capacity and favorable to be a candidate of electrode materials for supercapacitor [23]. The electrochemical reactions between $rGO_{10}-CoNi_2S_{4-x}$ electrode materials and the electrolyte can be elucidated as follows [24]:

$$CoNi_2S_4+2OH^- \rightleftharpoons CoS_{2x}OH+Ni_2S_{4-2x}OH+2e \quad (1)$$

The intrinsic energy storage process of $rGO_{10}-CoNi_2S_{4-x}$ in alkaline electrolytes primarily involves irreversible phase shifts, surface adsorption and partly reversible energy storage processes [6]:

$$CoNi_2S_{4-x}+\frac{3x}{2}OH^- \rightleftharpoons (CoNi_2)_{1-\frac{x}{4}}S_{4-x}+\frac{x}{2}Ni(OH)_2+\frac{x}{4}Co(OH)_2+\frac{3x}{2}e \quad (2)$$

$$(CoNi_2)_{1-\frac{x}{4}}S_{4-x}+(38-\frac{19x}{2})OH^- \rightleftharpoons (2-\frac{x}{2})Ni(OH)_2+(1-\frac{x}{4})Co(OH)_2+(4-x)SO_4^{2-}+(16-4x)H_2O+(30-\frac{15}{2})e \quad (3)$$

$$Co(OH)_2+OH^- \rightleftharpoons CoOOH+H_2O+e \quad (4)$$

$$Ni(OH)_2+OH^- \rightleftharpoons NiOOH+H_2O+e \quad (5)$$

GCD measurement is an effective method to study the energy storage capabilities of electrode materials. Figure 9(c) depicts the GCD test results for $CoNi_2S_4$ and $rGO_{10}-CoNi_2S_{4-x}$ at 1 A/g. Due to the formation of sulfur vacancies as confirmed in

Figs. 5(b) and S1 in SI, $rGO_{10}-CoNi_2S_{4-x}$ electrode has longer discharge time than $CoNi_2S_4$ electrode, indicating that more charges can be stored for the $rGO_{10}-CoNi_2S_{4-x}$ electrode than $CoNi_2S_4$, well consistent with CV results. It can be seen that for both samples, the obvious charging and discharging voltage platforms demonstrate the existence of the Faraday process, good correlation with CV results in Figs. 9(b) and Fig. S2(a) in SI. Moreover, the nearly symmetric charge−discharge profiles further demonstrate the highly reversible for the Faradaic redox reactions, as indicated by Reactions (2)−(5). Figures 9(d) and S2(b) in SI demonstrate the GCD curves of $rGO_{10}-CoNi_2S_{4-x}$ and $CoNi_2S_4$ throughout current densities of 1−30 A/g, respectively. All the GCD curves at different current densities remain almost the similar shapes for each sample, revealing the outstanding reversibility and rate performance. The discharge time of $rGO_{10}-CoNi_2S_{4-x}$ is longer than that of $CoNi_2S_4$, indicating the efficient charge storage and transport. The C_s values shown in Fig. 10 were obtained from the charge−discharge profiles by Eq. (S1) in SI, and the corresponding C_s values of $rGO_{10}-CoNi_2S_{4-x}$ can reach 3050.1, 2999.3, 2809.7, 2625.5, 2368.3 and 2199.5 F/g at current densities of 1, 2, 5, 10, 20 and 30 A/g, respectively. These results are much higher than those of $CoNi_2S_4$ (2356.5, 1989.5, 1587.4, 1252.6, 868.0 and 557.5 F/g) under the corresponding current densities. Remarkably, with the current density increasing from 1 to 10 A/g, the specific capacitance of $rGO_{10}-CoNi_2S_{4-x}$ still maintains 86.1% at 10 A/g, which is higher than that of $CoNi_2S_4$ (53.2%), indicating the excellent rate performance. This can be explained as follows: on the one hand, the open sheet structure of $rGO_{10}-CoNi_2S_{4-x}$ in Fig. 2(d) can facilitate the fast transport of ions. On the other hand, the formation of sulfur vacancies in $rGO_{10}-CoNi_2S_{4-x}$ composite electrode can provide the fast redox rate and good conductivity, thus enhancing the specific capacitance retention.

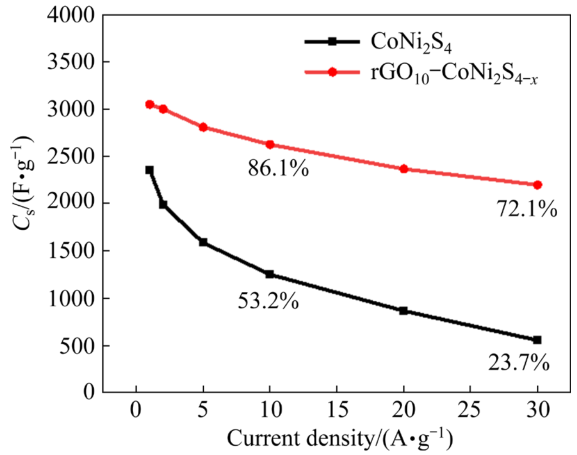

Fig. 10 C_s values of $rGO_{10}-CoNi_2S_{4-x}$ and $CoNi_2S_4$ at different current densities

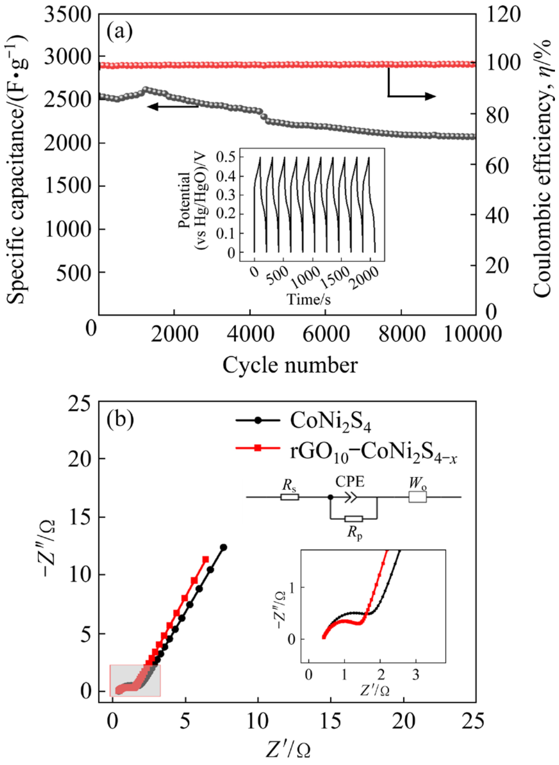

Fig. 11 Cycling stability of $rGO_{10}-CoNi_2S_{4-x}$ at 10 A/g for 10000 cycles (Inset: GCD curve of final 10 cycles) (a) and EIS curves of $rGO_{10}-CoNi_2S_{4-x}$ and $CoNi_2S_4$ (b)

The long cycling life is very essential for supercapacitor applications. Figure 11(a) displays specific capacitance and coulombic efficiency obtained from the repeated GCD measurements at 10 A/g. The coulombic efficiency is also called the charge−discharge efficiency (η), which is defined as $\eta=(t_d/t_c)\times100\%$, where t_d and t_c are the charge and discharge time, respectively. Following 10000 charge−discharge cycles, the coulombic efficiency of $rGO_{10}-CoNi_2S_{4-x}$ keeps about 100%, and the capacitance retention still maintains 81.5% of its original value, indicating remarkable cycle stability and excellent electrochemical reversibility during the long-term cycle performance. The excellent electrochemical properties are of great significance for high-energy hybrid supercapacitors. Owing to the delayed activation during the cycles, the C_s of

rGO_{10}−$CoNi_2S_{4-x}$ increases a little bit for the first 2000 cycles, similar phenomena have been reported in Refs. [11,25]. The inset of Fig. 11(a) shows the charge−discharge curves for the last 10 cycles at 10 A/g, and the curve shape keeps almost unchanged, indicating good reversibility. For comparison, the η and cycling performance of $CoNi_2S_4$ are shown in Fig. S3 in SI. The calculated capacitance maintains almost 73.2% of its original value and coulombic efficiency is about 97.1% after 10000 cycles. The excellent performance of rGO_{10}−$CoNi_2S_{4-x}$ is closely correlated with the foamed nickel-supported porous sheet-like nanostructures of composite, which can greatly enhance the specific surface area and promote the transport of ions [26]. Meanwhile, the combination of graphene can effectively prevent the aggregation and volume expansion and contraction of composites during charging and discharging processes.

The charge transfer and ion diffusion mechanisms at the interface of electrolyte/electrode can be examined by EIS measurements. The impedance measurements of the rGO_{10}−$CoNi_2S_{4-x}$ and $CoNi_2S_4$ nanosheets were performed in the frequency range of $0.01-10^5$ Hz. Figure 11(b) illustrates the Nyquist plots of rGO_{10}−$CoNi_2S_{4-x}$ and $CoNi_2S_4$ nano-composites together with the equivalent circuit, which comprises bulk solution resistance R_s, charge transfer resistance, constant phase element (CPE), polarization resistance R_p and Warburg impedance W_o. For two samples, both plots are composed of the semicircles and straight lines in the high and low frequency regions, respectively. The rGO_{10}−$CoNi_2S_{4-x}$ electrode material has a lower R_s value of 0.404 Ω than $CoNi_2S_4$ (0.459 Ω), as obtained from the intercept of the Nyquist diagram with the real axis, suggesting that rGO_{10}−$CoNi_2S_{4-x}$ electrode material owns fast electron transport kinetics at the interface of electrode and electrolyte [23]. Charge transfer resistance is represented by the semicircular diameter and corresponds to the interface resistance between active electrode materials and electrolyte. As can be seen from Fig. 11(b), rGO_{10}−$CoNi_2S_{4-x}$ electrode material has a smaller semicircle compared to $CoNi_2S_4$, demonstrating that charge transfer resistance value of the rGO_{10}−$CoNi_2S_{4-x}$ (1.068 Ω) electrode material is lower than that of $CoNi_2S_4$ (1.398 Ω). The lower charge transfer resistance value represents the more effective electrolyte/ion diffusion and faster charge transfer in the diffusion process [25]. The lower charge transfer resistance of rGO_{10}−$CoNi_2S_{4-x}$ electrode material can be attributed to the following reasons: firstly, rGO is well known to be a good electrical conductor, which can offer a low-resistive pathway for electrons, thus accelerating the reaction kinetics. Secondly, the existence of sulfur vacancies in rGO_{10}−$CoNi_2S_{4-x}$ nano-composite is beneficial to the conductive contact between the nanosheets, as illustrated in Fig. 2(d) [13].

To gain an insight of electrochemical energy storage mechanism of rGO_{10}−$CoNi_2S_{4-x}$, the diffusion-controlled and capacitance-controlled current contributions are investigated by the CV curves, as shown in Fig. 12(a). The current response can be described according to Eqs. (6) and (7) [27,28]:

$$I=av^b \tag{6}$$

$$\lg I=b\lg v+\lg a \tag{7}$$

where I (mA) is the sum of the diffusion-controlled current ($I_{\rm diff}$) and the capacitance-controlled current ($I_{\rm cap}$), v (mV/s) is the scan rate, and a and b mean adjustable parameters. The value of b is the slope of the linear fit of $\lg I$ vs $\lg v$. Typically, b=0.5 means the diffusion-controlled process, and b=1 suggests capacitive response. The slopes calculated from the linear fitting in Fig. S4 in SI related to the anode and cathode b values are 0.677 and 0.675, respectively. This indicates that the capacitance contributions originate from both the extrinsic capacitive and intrinsic diffusional charge−storage. The stored charge can be quantified based on Eq. (8) [29,30]:

$$I=I_{\rm cap}+I_{\rm diff}=k_1v+k_2v^{1/2} \tag{8}$$

where k_1v and $k_2v^{1/2}$ represent the capacitance and diffusion-controlled processes, respectively. k_1 and k_2 are the constants and can be obtained by plotting fitting lines of $I/v^{1/2}$ versus $v^{1/2}$, respectively. The capacitance contribution of rGO_{10}−$CoNi_2S_{4-x}$ at 10 mV/s is 58% (orange area). Meanwhile, the capacitive contributions for rGO_{10}−$CoNi_2S_{4-x}$ at different scan rates are shown in Figs. 12(b) and S5 in SI, respectively. It can be obviously found that the capacitance contribution increases rapidly from 47% at the scan rate of 1 mV/s to 85% at 30 mV/s. The high capacitance contribution is essential to achieve the fast electrochemical kinetics for electrode

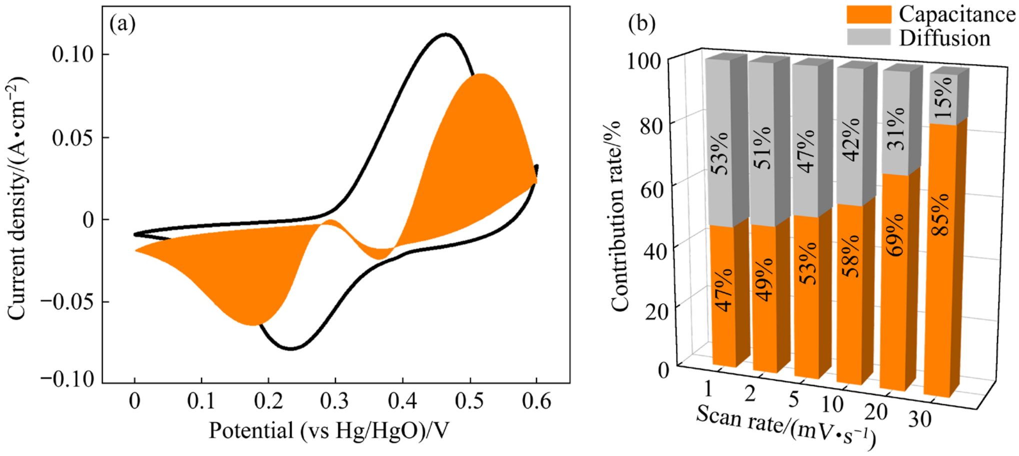

Fig. 12 Capacitance contribution of rGO_{10}−$CoNi_2S_{4-x}$ at scan rate of 10 mV/s (orange area) (a) and capacitance and diffusion distribution of rGO_{10}−$CoNi_2S_{4-x}$ at different scan rates

material in supercapacitors [31]. The larger capacitive contribution at higher scan rates can be attributed to the abundant porosity structure as illustrated in Fig. 6(b) and the introduction of sulfurs vacancies. Thus, high capacitance contributions are expected to improve electro-chemical performance and enhance stability.

3.3 Electrochemical performance of device

To further explore the realistic applications of the prepared rGO_{10}−$CoNi_2S_{4-x}$ electrode materials on the supercapacitors, the rGO_{10}−$CoNi_2S_{4-x}$//AC hybrid ASC was built. Figure 13 schematically illustrates the structure and working mechanism of ASC, in which rGO_{10}−$CoNi_2S_{4-x}$, AC and 3 mol/L KOH are employed as positive, negative materials and electrolyte, respectively, one piece of cellulose paper is used as the separator. The mass ratio of the positive to negative electrodes is 1:11 based on the charge balance principle, as calculated by Eq. (S2) in SI.

The activated carbon is often employed as the anode material for energy storage devices, here the electrochemical properties of AC were examined with three-electrode work station. All the CV curves in Fig. S6(a) in SI present an ideal rectangular shape and keep almost unchanged in the scan rate range of 1−50 mV/s, indicating the rapid response behavior of ions and the capacitive characteristic. The GCD curves in Fig. S6(b) in SI at current densities of 1−10 A/g are approximately symmetric triangular, manifesting the typical capacitive performance. The obtained C_s values from GCD measurements in Fig. S6(c) in SI are 137, 129, 123, 118, 114 and 111 F/g at 1, 2, 4, 6, 8 and 10 A/g, respectively. Good conductivity can be revealed by smaller resistance shown in Fig. S6(d) in SI with smaller resistance. Thus, AC is expected to be an ideal anode material for SCs.

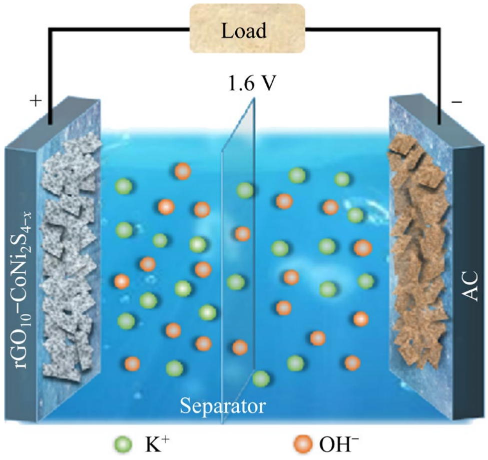

Fig. 13 Schematic illustration of assembled rGO_{10}−$CoNi_2S_{4-x}$//AC ASC

Figure 14 depicts CV curves of rGO_{10}−$CoNi_2S_{4-x}$ and AC electrodes with the corresponding working voltage of 0−0.6 V and −1−0 V, respectively. As a result, 1.6 V is expected to be the stable potential window for rGO_{10}−$CoNi_2S_{4-x}$//AC ASC. The CV curves in Fig. 15(a) of rGO_{10}−$CoNi_2S_{4-x}$//AC device were obtained under different potential windows within 1.2−1.9 V to evaluate the optimal working voltage. It can be obviously seen that all the CV curves keep the ideal shape under the desired potential window of 1.6 V. The curves become significantly polarized when the voltage exceeds 1.7 V, which may result from the oxygen evolution reaction of the aqueous electrolyte [32].

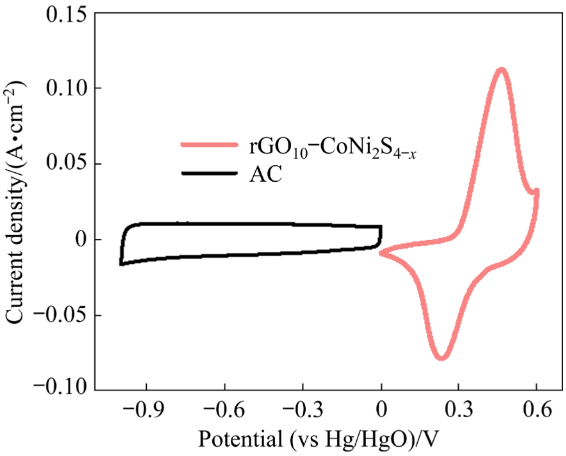

Fig. 14 CV curves of rGO$_{10}$−CoNi$_2$S$_{4-x}$ and AC electrodes at scan rate of 10 mV/s

Thus, the electrochemical properties of rGO$_{10}$−CoNi$_2$S$_{4-x}$//AC ASC were further characterized at the achieved voltage 1.6 V. Figure 15(b) provides the CV curves of rGO$_{10}$− CoNi$_2$S$_{4-x}$//AC ASC in the scan speed range of 1−50 mV/s, which reveals a quasi-rectangular shape with the prominent redox peaks. All the CV curves keep almost the same shape at different scan rates, demonstrating invertible and fast charge and discharge characteristics. Figure 15(c) illustrates the GCD curves detected at different current densities. The quasi-symmetrical shape manifests the capacitive behavior originating from rGO$_{10}$−CoNi$_2$S$_{4-x}$ nanocomposite, good consistent with the results shown in Fig. 12(b). The obtained C_s of rGO$_{10}$−CoNi$_2$S$_{4-x}$// AC ASC is 226 F/g at 1 A/g, and it maintains a capacitance retention of 60.6% at 10 A/g (137 F/g at 10 A/g) as in Fig. 15(d), implying excellent reversibility. Figure 16(a) shows the Nyquist diagram of the ASC within a frequency range from 10^{-2} to 10^5 Hz. To obtain EIS data, an equivalent circuit is established (the inset) and the calculated R_s value is 1.5 Ω, reflecting the low solution resistance.

Figure 16(b) illustrates the cycling performance of rGO$_{10}$−CoNi$_2$S$_{4-x}$//AC ASC. The capacitance retention reaches as high as 86.6% even after 10000 consecutive charge−discharge cycles at a current

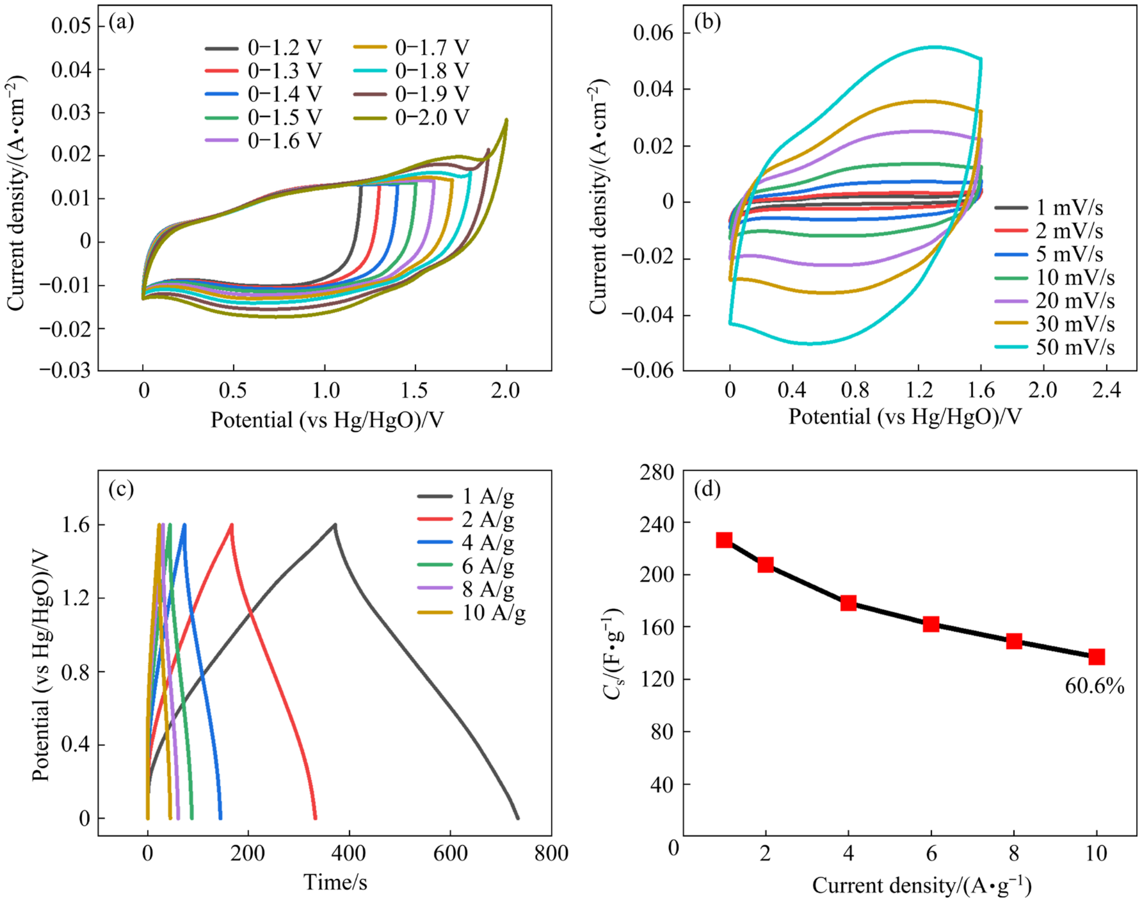

Fig. 15 CV curves of rGO$_{10}$−CoNi$_2$S$_{4-x}$//AC ASC at various potential windows and 10 mV/s (a), CV curves at 1−50 mV/s (b), GCD curves of rGO$_{10}$−CoNi$_2$S$_{4-x}$//AC ASC in current intensity range of 1−10 A/g (c), and C_s values of rGO$_{10}$−CoNi$_2$S$_{4-x}$//AC ASC at different current densities (d)

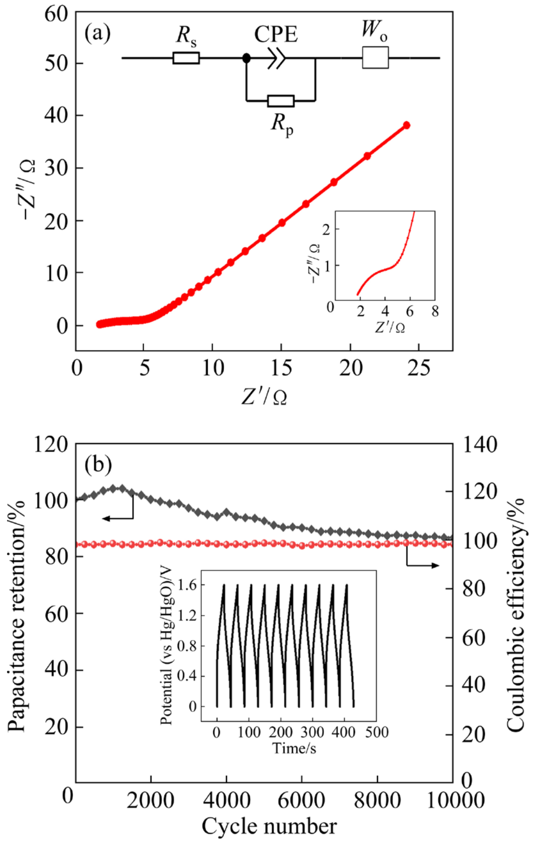

Fig. 16 EIS curve (a) and cycling performance of last 10 cycles (inset) at current density of 10 A/g (b) for rGO$_{10}$−CoNi$_2$S$_{4-x}$//AC ASC

density of 10 A/g, indicating the excellent cycling stability. However, the de-sulphuration reaction between cobalt nickel sulfide and OH$^-$ will cause the irreversible capacitance, resulting in the slight decrease of the capacitance retention. In the first 2500 cycles, due to the slow activation of the electrode, the capacitance rises a little bit and then falls until the steady state. Similar phenomena were reported in Refs. [25,33]. At the same time, it can also be found that coulombic efficiency always keeps 100% over the entire measurements, demonstrating the outstanding reversibility of the constructed device. This can be ascribed to the sufficient electrolyte penetration from the stacked nanosheet structure in the cycle process.

It is well known that both the energy density and power density are the very key parameters to evaluate the performance of energy storage devices. The energy density and power density of ASC can be calculated from Eqs. (S3) and (S4) in SI, as displayed by the Ragone diagrams in Fig. 17. The rGO$_{10}$−CoNi$_2$S$_{4-x}$//AC ASC achieves a high energy density of 80.35 W·h/kg at a power density 800 W/kg, and it still exhibits a high energy density up to 52.98 W·h/kg even at a power density 6400 W/kg. In this work, the as-constructed rGO$_{10}$−CoNi$_2$S$_{4-x}$//AC ASC presents the much higher energy density and power density than the reported CoNiS-based asymmetric supercapacitors [21,34−37]. For a clearer comparison, Table S2 in SI lists the present work and reported energy storage properties of cobalt-nickel sulfides. The excellent electrochemical performance of rGO$_{10}$−CoNi$_2$S$_{4-x}$// AC ASC mainly stems from the porous nanosheet cathode materials, which can supply sufficient charge transfer paths to promote Faraday redox reactions [38]. Meanwhile, the open nanostructure and the formed sulfur vacancies in rGO$_{10}$− CoNi$_2$S$_{4-x}$ can store much more charge [39]. Furthermore, the as-construed rGO$_{10}$−CoNi$_2$S$_{4-x}$// AC ASC can easily drive a bulb at a working voltage of 1.5 V, as shown in Fig. S7 is SI, suggesting its practical applications to the supercapacitor.

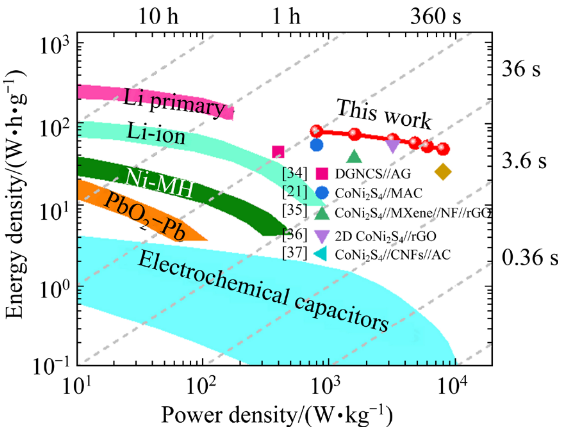

Fig. 17 Ragone plot of this work together with reported results

4 Conclusions

(1) The porous nanosheet rGO$_n$−CoNi$_2$S$_{4-x}$ composites with sulfur vacancies were synthesized through two-step hydrothermal procedure and a single-step reduction reaction.

(2) The formation of sulfur vacancies in rGO$_n$−CoNi$_2$S$_{4-x}$ composite can be confirmed by ESR results and Raman spectra.

(3) The fabricated rGO$_{10}$−CoNi$_2$S$_{4-x}$//AC ASC delivers a high energy density of 80.35 W·h/kg at a power density of 800 W/kg and excellent

cycling stability (86.6%) ever after 10000 consecutive charge−discharge cycles at a high current density of 10 A/g.

CRediT authorship contribution statement

Xu WANG: Conceptualization, Methodology, Investigation, Structural and electrochemical measurements, Writing − Original draft; **Bo-wang ZHAO:** SEM and TEM measurements, Writing – Review & editing; **Jia-yu LIANG:** XRD and Raman measurements, Writing – Review & editing; **Geng-zheng LIU:** XPS measurements, Writing − Review & editing; **Ze-fei GUO:** TEM measurements, Writing − Review & editing; **Hui-lian HAO:** Resources, Writing – Review & editing, Supervision, Data curation; **Wen-yao LI:** Resources, Writing – Review & editing; **Wen-zhong SHEN:** Supervision, Data curation.

Declaration of competing interest

The authors declare that they have no known competing financial interests or personal relationships that could have appeared to influence the work reported in this paper.

Acknowledgments

This work was supported by the Open Project of Key Laboratory of Artificial Structures and Quantum Control (Ministry of Education), Shanghai Jiao Tong University, China (No. 201301), and Class III Peak Discipline of Shanghai — Materials Science and Engineering (High-energy Beam Intelligent Processing and Green Manufacturing), China.

Supporting Information

Supporting information in this paper can be found at: http://tnmsc.csu.edu.cn/download/17-p0563-2023-0747-Supporting_Information.pdf.

References

[1] DEEPI A S, NESARAJ A S. Design of best performing hexagonal shaped Ag@CoS/rGO nanocomposite electrode material for electrochemical supercapacitor application [J]. Transactions of Nonferrous Metals Society of China, 2020, 30(10): 2764−2774.

[2] MA Bei-bei, CHEN Shui-jiao, HUANG Ye-wei, NIE Zhen-zhen, QIU Xiao-bin, XIE Xiu-qiang, WU Zhen-jun. Electrochemical lithium storage performance of three-dimensional foam-like biocarbon/MoS_2 composites [J]. Transactions of Nonferrous Metals Society of China, 2021, 31(1): 255−264.

[3] CAI Ke-xing, LUO Shao-hua, CONG Jun, LI Kun, YAN Sheng-xue, HOU Peng-qing, WANG Qing, ZHANG Ya-hui, LIU Xin. Enhancement of lithium storage performance of $ZnMn_2O_4$ anode by optimizing hydrothermal synthesis [J]. Transactions of Nonferrous Metals Society of China, 2023, 33(9): 2772−2783.

[4] ZHOU Ji, ZHANG Li-na, LIU Bin-bin, XU Cai-xia, LIU Hong. Preparation of hollow core-shelled $MnCoSe_x$/MnO@nitrogen-doped carbon composite by multiple interfaces coupling and its electrochemical properties [J]. Transactions of Nonferrous Metals Society of China, 2023, 33(8): 2471−2482.

[5] XU Ya-zhou, PENG Meng-ke, ZHANG Kai-yang, WANG Li, CHEN Jie-rui, HU Ting, YUAN Kai. From crystalline to partially amorphous: A facile strategy toward sulfur vacancy-enriched $CoNi_2S_4$ nanosheets with improved supercapacitor performance [J]. Advanced Sustainable Systems, 2022, 6(1): 2100414.

[6] LIU Yan-peng, WEN Yu-xiang, ZHANG Ya-nan, WU Xiao-gang, LI Hao-qian, CHEN Hang-da, HUANG Juan-juan, LIU Guo-han, PENG Shang-long. Reduced $CoNi_2S_4$ nanosheets decorated by sulfur vacancies with enhanced electrochemical performance for asymmetric supercapacitors [J]. Science China Materials, 2020, 63(7): 1216−1226.

[7] WANG Xiao-kun, PAN Yun, WANG Xiao-hong, GUO Ya-ning, NI Cheng-hao, WU Jing-bo, HAO Chen. High performance hybrid supercapacitors assembled with multi-cavity nickel cobalt sulfide hollow microspheres as cathode and porous typha-derived carbon as anode [J]. Industrial Crops and Products, 2022, 189: 115863.

[8] HAO Chen, NI Cheng-hao, WANG Xiao-kun, PAN Yun, WU Qian-qian, WU Jing-bo, WANG Xiao-hong. Fabrication of three-dimensional CuS_2@$CoNi_2S_4$ core–shell rod-like structures as cathode and thistle-derived carbon as anode for hybrid supercapacitors [J]. Chemical Engineering Journal, 2023, 465: 143024.

[9] HE Han-bing, LIU Zhen, PENG Chao-qun, LIU Jun, WANG Xiao-feng, ZENG Jing. 3D MoS_2/graphene nanoflowers as anode for advanced lithium-ion batteries [J]. Transactions of Nonferrous Metals Society of China, 2022, 32(12): 4041−4049.

[10] XIONG Ting, YU Zhi-gen, WU Hai-jun, DU Yong-hua, XIE Qi-dong, CHEN Jing-sheng, ZHANG Yong-wei, PENNYCOOK S J, LEE W S V, XUE Jun-min. Defect engineering of oxygen-deficient manganese oxide to achieve high-performing aqueous zinc ion battery [J]. Advanced Energy Materials, 2019, 9(14): 1803815.

[11] LIU Rui-qi, XU Shu-sheng, SHAO Xiao-xuan, WEN Yi, SHI Xue-rong, HUANG Li-ping, HONG Min, HU Jing, YANG Zhi. Defect-engineered NiCo−S composite as a bifunctional electrode for high-performance supercapacitor and electrocatalysis [J]. ACS Applied Materials & Interfaces, 2021, 13(40): 47717−47727.

[12] LIU Ting-ting, PENG Na, ZHANG Xi-kun, ZHENG Run-tian, XIA Mao-ting, YU Hao-xiang, SHUI Miao, XIE Ying, SHU Jie. Controllable defect engineering enhanced bond strength for stable electrochemical energy storage [J]. Nano Energy, 2021, 79: 105460.

[13] QIAN Xing-yue, YIN Yi-xuan, LU Yu-chen, XIA Jia-wei, HUANG Bing-ji, SUN Jing-wen, HE Guang-yu, CHEN

Hai-qun. Construction of sulfur vacancies enriched hollow zinc cobalt bimetallic sulfides for high-performance supercapacitors [J]. Journal of Alloys and Compounds, 2022, 913: 165191.

[14] GUO Ya-ning, HAO Chen, WANG Xiao-kun, YANG Ying, WANG Xiao-hong, WU Jing-bo, SHEN Yu-tang. Facile fabrication of CoNi-layered double hydroxide/$NiCo_2S_4$/reduced graphene oxide composites by in situ hydrothermal growth strategy for supercapacitor performance [J]. Ceramics International, 2022, 48(12): 17644−17653.

[15] NAN Hao-shan, LIU Miao, ZHANG Wei-jin, ZHANG Qi, XU Jian, HU Xiao-ying, TIAN Hong-wei. One-step synthesis of $NiCo_2S_4$ with high electrochemical performance used for hybrid capacitor [J]. Journal of Alloys and Compounds, 2020, 832: 155037.

[16] KANG Ling, ZHANG Meng-yao, ZHANG Jian, LIU Shu-de, ZHANG Nan, YAO Wen-jing, YE Yan, LUO Chen, GONG Zhi-wei, WANG Chao-lun, ZHOU Xiao-feng, WU Xing, JUN Seong-chan. Dual-defect surface engineering of bimetallic sulfide nanotubes towards flexible asymmetric solid-state supercapacitors [J]. Journal of Materials Chemistry A, 2020, 8(45): 24053−24064.

[17] LU Fei, ZHOU Min, LI Wan-rong, WENG Qun-hong, LI Cui-ling, XUE Yan-ming, JIANG Xiang-fen, ZENG Xiang-hua, BANDO Y, GOLBERG D. Engineering sulfur vacancies and impurities in $NiCo_2S_4$ nanostructures toward optimal supercapacitive performance [J]. Nano Energy, 2016, 26: 313−323.

[18] YANG Ying, WANG Dao-rui, WANG Yuan-yuan, LI Ze-lin, SU Rui, WANG Xin, XU Tong, WANG Shuang-xi. Sulfur vacancy-rich carbonaceous Co_9S_8−ZnS nanotubes for the oxygen evolution reaction [J]. ACS Applied Energy Materials, 2022, 5(12): 14869−14880.

[19] LU Xue-feng, ZHANG Song-lin, SIM W L, GAO Shu-yan, LOU Xiong-wen. Phosphorized $CoNi_2S_4$ yolk-shell spheres for highly efficient hydrogen production via water and urea electrolysis [J]. Angewandte Chemie, 2021, 133(42): 23067−23073.

[20] SIVANANTHAM A, GANESAN P, SHANMUGAM S. Hierarchical $NiCo_2S_4$ nanowire arrays supported on Ni foam: An efficient and durable bifunctional electrocatalyst for oxygen and hydrogen evolution reactions [J]. Advanced Functional Materials, 2016, 26(26): 4661−4672.

[21] SIDDIQA A, NAGARAJU D H, PADAKI M. High-energy-density asymmetric supercapacitor based on layered-double-hydroxide-derived $CoNi_2S_4$ and eco-friendly biomass-derived activated carbon [J]. Energy & Fuels, 2022, 36(21): 13286−13295.

[22] WANG Jia-yang, SHEN Yong-li, WEI Gui-juan, XI Wei, MA Xiao-ming, ZHANG Wei-qing, ZHU Pei-pei, AN Chang-hua. Synthesis of ultrathin Co_2AlO_4 nanosheets with oxygen vacancies for enhanced electrocatalytic oxygen evolution [J]. Science China Materials, 2020, 63(1): 91−99.

[23] WANG Pan, QI Ji, LI Chuang, LI Wen-ping, WANG Tong-hua, LIANG Chang-hai. Hierarchical $CoNi_2S_4$@NiMn-layered double hydroxide heterostructure nanoarrays on superhydrophilic carbon cloth for enhanced overall water splitting [J]. Electrochimica Acta, 2020, 345: 136247.

[24] NAN Hao-shan, LIU Miao, ZHANG Qi, WANG Ming, LIU Shu-jie, QIAO Liang, HU Xiao-ying, TIAN Hong-wei. Intrinsic energy-storage mechanism of low crystallinity nickel-cobalt sulfide as anode material for supercapacitors [J]. Journal of Power Sources, 2020, 451: 227822.

[25] XU Shu-sheng, LIU Rui-qi, SHI Xue-rong, MA Yu-jie, HONG Min, CHEN Xin-wei, WANG Tao, LI Fang-jie, HU Nan-tao, YANG Zhi. A dual CoNi MOF nanosheet/nanotube assembled on carbon cloth for high performance hybrid supercapacitors [J]. Electrochimica Acta, 2020, 342: 136124.

[26] ZU Lian-hai, ZHANG Wei, QU Long-bing, LIU Liang-liang, LI Wei, YU Ai-bing, ZHAO Dong-yuan. Mesoporous materials for electrochemical energy storage and conversion [J]. Advanced Energy Materials, 2020, 10(38): 2002152.

[27] QU Zi-han, LI Jian-chen, GUO Man-ying, ZHAO Li-jun, DUAN Lian-feng, DING Shan-shan. Design tremella-like Ni−Co selenide with wonderful electrochemical performances as supercapacitor cathode material [J]. Electrochimica Acta, 2021, 393: 139049.

[28] ZHAO Yue, HAO Hui-lian, SONG Tian-liang, WANG Xu, LI Chang-wang, LI Wen-yao. High energy-power density Zn-ion hybrid supercapacitors with N/P Co-doped graphene cathode [J]. Journal of Power Sources, 2022, 521: 230941.

[29] YANG Qing-jun, LIU Yu, DENG Cheng-yu, SUN Lin, SHI Wei-dong. In-situ construction of heterostructure $(Ni,Co)Se_2$ nanoarrays derived from cone-like ZIF-L for high-performance hybrid supercapacitors [J]. Journal of Colloid and Interface Science, 2022, 608: 3049−3058.

[30] MAHMOOD A, ZHAO Bo-lin, JAVED M S, HE De-quan, CHEONG W C, HAN Dong-xue, NIU Li. Unprecedented dual role of polyaniline for enhanced pseudocapacitance of cobalt–iron layered double hydroxide [J]. Macromolecular Rapid Communications, 2022, 43(7): e2100905.

[31] LI Yang, YANG Wang, YANG Wu, WANG Zi-qi, RONG Jian-hua, WANG Guo-xiu, XU Cheng-jun, KANG Fei-yu, DONG Liu-bing. Towards high energy and anti-self-discharge Zn-ion hybrid supercapacitors with new understanding of the electrochemistry [J]. Nano-Micro Letters, 2021, 13: 1−16.

[32] ZHAO Jian, LI Zhen-jiang, SHEN Tong, YUAN Xiang-cheng, QIU Guan-hao, JIANG Qing-yan, LIN Yu-sheng, SONG Guan-ying, MENG Alan, LI Qing-dang. Oxygen-vacancy Bi_2O_3 nanosheet arrays with excellent rate capability and $CoNi_2S_4$ nanoparticles immobilized on N-doped graphene nanotubes as robust electrode materials for high-energy asymmetric supercapacitors [J]. Journal of Materials Chemistry A, 2019, 7(13): 7918−7931.

[33] DUAN Zhi-chang, SHI Xue-Rong, SUN Chun-yan, LIN Wen-song, HUANG Si-min, ZHANG Xiang-rui, HUANG Meng-ru, YANG Zhi, XU Shu-sheng. Interface engineered hollow Co_3O_4@$CoNi_2S_4$ nanostructure for high efficiency supercapacitor and hydrogen evolution [J]. Electrochimica Acta, 2022, 412: 140139.

[34] JING Chuan, GUO Xiao-long, XIA Lu-hao, CHEN Yu-xiang, WANG Xin, LIU Xiao-ying, DONG Bi-qin, DONG Fan, LI Shao-chun, ZHANG Yu-xin. Morphologically confined hybridization of tiny $CoNi_2S_4$ nanosheets into S, P Co-doped graphene leading to enhanced pseudocapacitance and rate capability [J]. Chemical Engineering Journal, 2020, 379: 122305.

[35] RUAN Chen-ya, ZHU Dong-dong, QI Ji-qiu, MENG Qing-kun, WEI Fu-xiang, REN Yao-jian, SUI Yan-wei, ZHANG Hao. MXene-modulated CoNi$_2$S$_4$ dendrite as enhanced electrode for hybrid supercapacitors [J]. Surfaces and Interfaces, 2021, 25: 101274.

[36] ZHANG Kai-yang, WEI Yuan-hao, HUANG Jun, XIAO Ying-bo, YANG Wei-zu, HU Ting, YUAN Kai, CHEN Yi-wang. A generalized one-step in situ formation of metal sulfide/reduced graphene oxide nanosheets toward high-performance supercapacitors [J]. Science China Materials, 2020, 63(10): 1898−1909.

[37] ZHU Jun-sheng, HAN Chen-chen, SONG Xiao-yu. Facile synthesis of novel CoNi$_2$S$_4$/carbon nanofibers composite for high-performance supercapacitor [J]. Materials Chemistry and Physics, 2022, 283: 126038.

[38] LIU Ya-jun, ABDIRYIM T, JAMAL R, LIU Xiong, FAN Na-na, NIYAZ M, ZHANG Yao-long. High-performance quasi-solid-state hybrid supercapacitor for self-powered strain sensor based on poly(3,4-propylenedioxythiophene)/NiS$_2$@hollow carbon sphere composite and sulfonated cellulose hydrogel electrolyte [J]. Applied Surface Science, 2023, 608: 154989.

[39] CHENG Yan-hua, XU Zhi-hui, HAN Yue, LI Xiao-lan, ZHANG Si-wen, SUN Shi-shuai. Fabrication of sugar-coated CoNi$_2$S$_4$/Ni$_3$P nanostructure with ultrahigh electrochemical performance for supercapacitor application [J]. International Journal of Electrochemical Science, 2021, 16(4): 210440.

基于 rGO−CoNi$_2$S$_4$ 缺陷工程增强的非对称超级电容器的电化学性能

王 絮[1]，赵伯旺[1]，梁佳宇[1]，刘庚正[1]，郭泽飞[1]，郝惠莲[1]，李文尧[1]，沈文忠[2]

1. 上海工程技术大学 材料科学与工程学院，上海 201620；
2. 上海交通大学 物理与天文学院，上海 200240

摘　要：为了探索过渡金属硫化物中的硫缺陷对其负极材料电化学性能的影响，以氧化石墨烯(GO)和钴镍硫化物(CoNi$_2$S$_4$)为原料通过溶剂热法合成了含硫缺陷的还原氧化石墨烯−钴镍硫化物(rGO$_{10}$−CoNi$_2$S$_{4-x}$)复合电极材料。所合成的 rGO$_{10}$−CoNi$_2$S$_{4-x}$ 复合电极材料含有纳米片和纳米棒。恒电流充放电测试表明，当电流密度为 1 A/g 时，rGO$_{10}$−CoNi$_2$S$_{4-x}$ 电极材料的比电容为 3050.1 F/g；当电流密度从 1 A/g 增加至 10 A/g 时，倍率容量保持率为 86.1%。与不含硫缺陷的 rGO−CoNi$_2$S$_4$ 相比，含有硫缺陷的 rGO$_{10}$−CoNi2S$_{4-x}$ 具有较高的比电容和较好的倍率性能。优化后的含硫缺陷 rGO$_{10}$−CoNi$_2$S$_{4-x}$ 电极材料呈现良好的循环性能和倍率性能。

关键词：rGO$_{10}$−CoNi$_2$S$_{4-x}$ 复合材料；超级电容器；电化学性能；硫缺陷；溶剂热法

(Edited by Wei-ping CHEN)